Exceptional points in Fluid-Structure interaction

Javier Sierra-Ausin [1] and Olivier Marquet[2]

[1]DMPE, ONERA, Université de Toulouse, 31055 Toulouse, France

[2]DAAA, ONERA, Institut Polytechnique de Paris, 92190 Meudon, France

Corresponding author: Javier Sierra-Ausin, javier.sierra_ausin@onera.fr

(Received xx; revised xx; accepted xx)

The linear stability analysis of fluid-structure interaction (FSI) systems, governed by inherently non-Hermitian operators, can exhibit spectral singularities known as exceptional points (EPs). This study demonstrates the existence and topological consequences of EPs across three canonical aeroelastic configurations: vortex-induced vibration of a spring-mounted cylinder, flutter of a thin plate, and transonic flutter of an OAT15a airfoil. A unified numerical framework is employed, coupling the compressible Navier–Stokes equations with structural dynamics. Stability is analysed via a characteristic equation constructed from fluid transfer functions, efficiently interpolated into the complex plane using the Loewner framework. Results reveal second-order EPs (EP_2) where two eigenmodes coalesce, leading to characteristic eigenvalue veering and mode-swapping phenomena governed by a half-integer winding number. In the transonic case, the interaction of three modes (fluid/buffet, pitching, heaving) is organised by a third-order EP (EP_3), a codimension-four singularity where three eigenvalues and eigenvectors coalesce. These findings establish EPs as fundamental features in FSI, providing a novel topological perspective on stability transitions, with implications for predicting and controlling phenomena like flutter and the transonic dip.

Key words: Authors should not enter keywords on the manuscript, as these must be chosen by the author during the online submission process and will then be added during the typesetting process (see Keyword PDF for the full list). Other classifications will be added at the same time.

1. Introduction

The mathematical description of dissipative and open systems frequently necessitates a departure from the conservative, Hermitian framework that underpins much of classical physics. In fluid mechanics, this is the rule rather than the exception: the Navier-Stokes equations are inherently dissipative, and the linearised operators that arise in the study of stability, acoustics, and wave propagation are often non-normal (Trefethen *et al.* 1993). This non-normality leads to rich phenomena such as transient growth and sensitivity to perturbations, which are crucial for understanding the transition to turbulence (Schmid

2007) and the dynamics of coherent structures. A powerful and generalised framework for analysing such open systems has emerged from the study of non-Hermitian quantum mechanics and optics, where the spectrum of the governing non-self-adjoint operator is complex. Within this framework, a paramount feature is the existence of exceptional points (EPs)—spectral singularities where not only the eigenvalues but also the corresponding eigenvectors of the system coalesce (Heiss 2012; Bergholtz *et al.* 2021).

The topology of the complex energy Riemann surface around an EP leads to a host of counter-intuitive phenomena with no direct analogue in Hermitian systems. These include the chiral behaviour of state populations when an EP is dynamically encircled (Doppler *et al.* 2016), that is, encircling an EP in a clockwise or a counter-clockwise direction results in different final states. We also find the breakdown of the conventional bulk-boundary correspondence (Bergholtz *et al.* 2021), and the non-Hermitian skin effect—a phenomenon where a macroscopic number of states localise at a system's boundary, as first rigorously characterized in quantum systems (Yao & Wang 2018) and since explored in photonic (Zhou *et al.* 2018) and acoustic (Zhu *et al.* 2018) metamaterials. The implications of EPs are now being explored across a wide range of classical wave systems, including nanophotonics for light manipulation (Miri & Alu 2019), in single-mode lasers to decrease the fluctuating level of lasers Feng *et al.* (2014) or in augmenting the quality of sensors (Wiersig 2020) and in the design of electrical circuits (Helbig *et al.* 2020) where they have been shown to enable novel functionalities such as unidirectional invisibility, topological lasing, and enhanced sensing.

The exploration of non-Hermitian physics and EPs has attracted some interest in acoustics and thermoacoustics. In acoustics, where the concepts of gain and loss can be engineered with some precision, we find the seminal work by Shi *et al.* (2016) who demonstrated the accessibility of EPs in parity-time (PT) symmetric acoustic systems, revealing phenomena like unidirectional transparency.The role of EPs has since been elucidated in sound absorption, with Achilleos *et al.* (2017) showing how they govern the behavior of non-Hermitian acoustic metamaterials, and Xiong *et al.* (2017) optimizing sound attenuation in metaporous materials by tuning them to an EP. The extension of these ideas to systems with background flow was established by Aurégan & Pagneux (2017), who explored PT-symmetric scattering in flow ducts. More recently, studies have continued to explore the implications of EPs in complex scattering scenarios (Matsushima & Yamada 2025) and in achieving extreme wave phenomena like asymmetric absorption in elastic structures (Li *et al.* 2022).

In the field of thermoacoustics Mensah *et al.* (2018) established the existence of EPs in a prototypical thermoacoustic system, demonstrating their signature infinite eigenvalue sensitivity. The interplay between different types of modes, such as those of pure acoustic origin and Intrinsic Thermoacoustic (ITA) modes, was further shown by Orchini *et al.* (2020) to generate EPs that govern the stability landscape by acting as spectral root loci. The profound implications for practical systems were highlighted by Ghani & Polifke (2021) who identified an EP in a combustion experiment, showing how its branch-switching characteristic can facilitate a sudden jump from strong instability to stable operation. This real-world impact underscores the critical need to understand EPs, as their presence can fundamentally affect the reliability of stability analyses, a point rigorously examined by Schaefer *et al.* (2021). The understanding of EPs is now being leveraged to develop innovative design methods for stable combustion systems. Recent research by Casel & Ghani (2024*a*,*b*) has introduced the Exceptional Point-based Thermoacoustic Design (EPTD) method. This conceptual framework, detailed in two parts, uses the relation between mode origins, encoded in the EP's position and parameters, to strategically shift the entire thermoacoustic spectrum toward stability. The EPTD method has been successfully

demonstrated in lab-scale combustors, stabilizing originally unstable laminar and turbulent flame configurations. Concurrently, the role of system symmetries in organizing these non-Hermitian degeneracies has been advanced by Humbert & Orchini (2025), who demonstrated how symmetry-breaking induces EPs in the complex spectra of annular combustors. This collective body of work represents a paradigm shift from traditional stability analysis toward actively designing stability maps using the topological features of EPs.

In hydrodynamics, the concepts underpinning non-Hermitian physics have long been in the analysis of linear stability and global modes (Chomaz 2005). However, EPs have scarcely been clearly identified and only recently their importance has been highlighted. Recently, Jouin *et al.* (2024) identified different types of EPs as the result of the interaction between cross-flow vortices with opposite spanwise wavenumber and different spanwise wavenumber. Kern *et al.* (2024) documented the formation of subharmonic eigenvalue orbits in the periodic spectrum of pulsating plane Poiseuille flow as the pulsation amplitude is increase, due to the coalescence of eigenvalues at exceptional points. Similarly, in the context of a rising bubble immersed in a liquid Bonnefis *et al.* (2024) identified a EP which results from the interaction of two symmetry breaking modes, the inclination-induced displacement and the lateral drift of the trajectory.

A particularly fertile and complex domain for the application of this non-Hermitian framework is the field of fluid-structure interaction (FSI). FSI systems are open and dissipative, characterised by a strong, often non-linear, coupling between a deformable or moving structure and a surrounding fluid flow. The linearised operators governing the stability of these coupled systems—such as in flutter of airfoils, vortex-induced vibrations, or the dynamics of flags and membranes—are inherently non-Hermitian. The spectral properties of these coupled fluid-structure operators are known to give rise to complex phenomena like mode coalescence in flutter bifurcations, which bears the hallmark of an EP. We posit that the confluence of two distinct non-normal subsystems—the fluid and the structure—creates a rich environment for the emergence and manipulation of EPs. Understanding these points in FSI is not merely a formal exercise; it holds the potential to unravel the mechanisms behind hard-to-predict instabilities, to design novel strategies for their suppression, and to exploit the unique spectral properties of EPs for applications in energy harvesting and flow control. In this paper, we therefore seek to elucidate the role of exceptional points in fluid-structure interaction, exploring their manifestation, topological consequences, and the distinctive physical phenomena they govern in this fundamentally coupled context.

We have selected three aeroelastic configurations in order to show the importance of EPs in fluid-structure interaction, these are: (a) the flow past a spring-mounted cylinder, which exhibits Vortex-Induced-Vibrations (VIV), (b) the flow past a thin plate at zero angle of attack, which exhibits flutter and (c) the transonic flow past an airfoil which exhibits transonic flutter. The last two configurations are the two-dimensional representation of the flutter dynamics of a wing-section, where the bending mode is represented as the heaving motion, while the torsion is modeled by the pitching motion. Both structural degrees of freedom are treated as a spring-mass-damper system: heaving is emulated by a vertical spring, and pitching by a torsional spring, as shown in fig. 1 (a).

2. Methods

We numerically integrate the conservative variables $\mathbf{Q} = \left(\rho, \mathbf{m}, \rho E\right)^T$, ρ the density field, $\mathbf{m} \equiv \rho\mathbf{u}$ the momentum field with $\mathbf{u}$ the velocity field, and ρE the total energy, according to the compressible Navier–Stokes equations. The governing equations are written in the

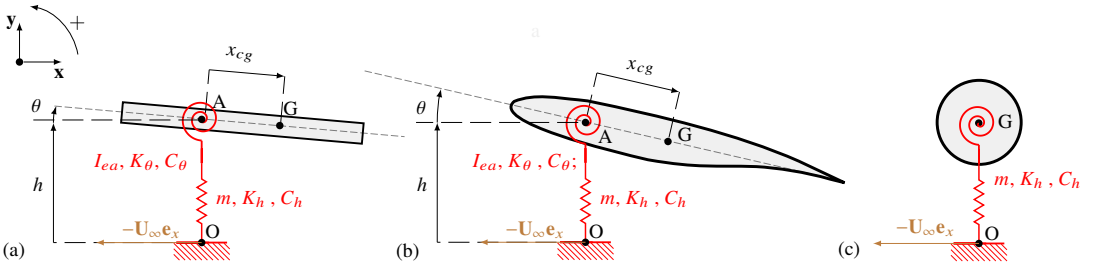

Figure 1. Diagram of the three aeroelastic configurations (a) Two-degrees of freedom spring-mounted plate. (b) Two degrees of freedom OAT15a airfoil. (c) Spring-mounted cylinder.

moving frame of reference using the absolute velocity formulation (Mougen and Magnaudet 2002), which can be written in compact form as follows:

$$\partial_t \mathbf{Q} + \nabla \cdot \mathbf{F}_c(\mathbf{Q}) - \nabla \cdot \mathbf{F}_v(\mathbf{Q}, \nabla \mathbf{Q}) = \mathbf{S}. \tag{2.1}$$

In eq. (2.1) the convective flux $\mathbf{F}_c(\mathbf{Q})$ is the one written in the absolute frame of reference but shifted with the relative velocity $\mathbf{w}$, that is as follows,

$$\mathbf{F}_c(\mathbf{Q}) = \begin{pmatrix} \rho(\mathbf{u}-\mathbf{w}) \\ \mathbf{m} \otimes (\mathbf{u}-\mathbf{w}) + p\mathbb{I} \\ (\mathbf{u}-\mathbf{w})(\rho E) + p\mathbf{u} \end{pmatrix}, \tag{2.2}$$

the source term includes the Coriolis force in the momentum equation

$$\mathbf{S}(\mathbf{Q}, \Omega) = \begin{pmatrix} 0 \\ -\rho \Omega \times \mathbf{u} \\ 0 \end{pmatrix}, \tag{2.3}$$

and finally the viscous flux

$$\mathbf{F}_v(\mathbf{Q}) = \begin{pmatrix} 0 \\ \tau(\mathbf{u}) \\ \kappa \nabla T + \tau(\mathbf{u}) \cdot \mathbf{u} \end{pmatrix}, \text{ with } \tau(\mathbf{u}) = \mu\Big[(\nabla \mathbf{u} + \nabla \mathbf{u}^T) - \frac{2}{3}\nabla \cdot \mathbf{u}\mathbb{I}\Big]. \tag{2.4}$$

The control parameters of the flow system are the Reynolds number Re_∞, which is the ratio between inertia and viscous forces, the Prandtl number Pr, which is the ratio between kinematic viscosity $\nu \equiv \mu/\rho$ and thermal diffusivity κ, and the Mach number M_∞, which is the ratio of the flow velocity and the speed of sound c_∞:

$$Re_\infty = \frac{\rho_\infty U_\infty L}{\mu}, \; Pr = \frac{\mu}{\rho\kappa}, \; M_\infty = \frac{U_\infty}{c_\infty} \tag{2.5}$$

In the configuration of the flow past a cylinder, fig. 1 (a), the reference length L is the diameter of the cylinder, while in the two others the reference length is the chord of the plate (fig. 1 (b)) and the airfoil (fig. 1 (c)) respectively. In the transonic flow past an airfoil the dynamic viscosity μ is replaced by the sum of the dynamic molecular viscosity and the dynamic turbulent viscosity $\mu + \mu_t$ where μ_t is obtained using the Spalart–Allmaras turbulence model using the compressibility and Edwards correction.

In order to model the aeroelastic motion of a wing, we simply consider a wing section. The bending mode is represented as free movement in the perpendicular direction to the incoming flow, labeled heaving, while torsion is modeled through a rotational degree of

freedom, labeled pitching. Both structural degrees of freedom are treated as a spring-mass-damper system: heaving is emulated by a vertical spring, and pitching by a torsional spring, as shown in fig. 1. Here, the pitching angle is defined in the mathematically positive direction, opposite to the commonly defined *pitch-up* angle of attack, with $\alpha = -\theta$. Both springs are mounted at the center of gravity, $x_{cg} = 0$, that is, the elastic center coincides with the center of gravity. We have made this choice to simplify the analysis, but it does not change the main conclusions. The system of ordinary differential equations is as follows:

$$\begin{aligned} m\frac{\partial^2 h}{\partial t^2} + C_h\frac{\partial h}{\partial t} + K_h h = L(\mathbf{Q}) &= \Big[\int_{\Gamma_{fs}} \big(-p\mathbb{I} + \tau(\mathbf{u})\big)\mathbf{n}\,\mathrm{d}\mathbf{x}\Big]\cdot \mathbf{R}^T(\theta)\mathbf{e}_y \\ I_{ea}\frac{\partial^2 \theta}{\partial t^2} + C_\theta\frac{\partial \theta}{\partial t} + K_\theta(\theta-\theta_s) = M(\mathbf{Q}) &= \Big[\int_{\Gamma_{fs}} \mathbf{x}\wedge\big(-p\mathbb{I} + \tau(\mathbf{u})\big)\mathbf{n}\,\mathrm{d}\mathbf{x}\Big]\cdot \mathbf{e}_z \end{aligned} \tag{2.6}$$

Here, m is the mass of the structure, I_{ea} is the moment of inertia around the elastic center, and the coefficients K_h, K_θ , C_h, and C_θ are the stiffness and damping coefficients, respectively. The angle θ_s is the pre-stress pitching angle, which represents the pre-stressed state of the system when the angle of attack is not null, that is, $\theta_s = -\alpha_0 - M(\mathbf{Q}_0)/K_\theta$.

$$\begin{aligned} \frac{\partial^2 h}{\partial t^2} + 2\zeta_h\Big(\frac{\Omega}{U^*}\Big)\frac{\partial h}{\partial t} + \Big(\frac{\Omega}{U^*}\Big)^2 h &= \frac{1}{\overline{m}}\frac{2}{\rho_\infty U_\infty^2 L}\Big[\int_{\Gamma_{fs}} \big(-p\mathbb{I} + \tau(\mathbf{u})\big)\mathbf{n}\,\mathrm{d}\mathbf{x}\Big]\cdot \mathbf{R}^T(\theta)\mathbf{e}_y \\ \frac{\partial^2 \theta}{\partial t^2} + 2\zeta_\theta\Big(\frac{1}{U^*}\Big)\frac{\partial \theta}{\partial t} + \Big(\frac{1}{U^*}\Big)^2(\theta-\theta_s) &= \frac{1}{\overline{m} r_\theta^2}\frac{2}{\rho_\infty U_\infty^2 L^2}\Big[\int_{\Gamma_{fs}} \mathbf{x}\wedge\big(-p\mathbb{I} + \tau(\mathbf{u})\big)\mathbf{n}\,\mathrm{d}\mathbf{x}\Big]\cdot \mathbf{e}_z \end{aligned} \tag{2.7}$$

where as in the VIV problem of the cylinder, we simply consider the heaving h motion. In eq. (2.2) we introduced the rigid-body velocity $\mathbf{w}$ which is defined as follows

$$\mathbf{w} \equiv \mathbf{R}(\theta)^T\big(-\mathbf{U}_\infty, \dot{h}\big) + \dot{\theta}\mathbf{e}_z \wedge \mathbf{x}, \tag{2.8}$$

where the first term accounts for the relative translational velocity, the second term for the heaving motion and the last term accounts for the rotation of the body. Here $\mathbf{R}(\theta)$ is a rotation matrix used to project the translational velocity onto the rotating axes. Finally, the fluid system is complemented with the following boundary conditions. An adiabatic no-slip, that is, $\mathbf{u} = \mathbf{w}$, boundary condtion is imposed at the body wall. At the inlet we impose a constant density ρ_∞ and null velocity field $\mathbf{u} = \mathbf{0}$. Whereas at the outlet we impose a constant pressure $p_\infty = r\rho_\infty T_\infty$, where r is the ideal gas constant of air and $T_\infty = 288.15K$.

In order to determine the onset of self-sustained oscillations, we consider the linearization of eq. (2.1) and eq. (2.7), which can be written in a compact formulation as follows,

$$\begin{aligned} &\Big(\mathcal{R}(\lambda)\Big)^{-1}\hat{\mathbf{q}} \equiv \Big(\lambda\mathbf{B} + D\mathbf{F}|_{\mathbf{q}_0}\Big)\hat{\mathbf{q}} = \mathbf{m}_\theta\theta + \mathbf{m}_{\dot{\theta}}\dot{\theta} + \mathbf{m}_{\dot{h}}\dot{h} \\ &\lambda\theta = \dot{\theta}, \quad \lambda h = \dot{h} \\ &\lambda\dot{\theta} + 2\zeta_\theta\Big(\frac{1}{U^*}\Big)\dot{\theta} + \Big(\frac{1}{U^*}\Big)^2\theta = \frac{1}{\overline{m} r_\theta^2}C_M(\hat{\mathbf{q}}) = \frac{1}{\overline{m} r_\theta^2}\mathbf{c}_m^T\hat{\mathbf{q}} \\ &\lambda\dot{h} + 2\zeta_h\Big(\frac{\Omega}{U^*}\Big)\dot{h} + \Big(\frac{\Omega}{U^*}\Big)^2 h = \frac{1}{\overline{m}}C_L(\hat{\mathbf{q}}) = \frac{1}{\overline{m}}\mathbf{c}_L^T\hat{\mathbf{q}} \end{aligned} \tag{2.9}$$

The operator $D\mathbf{F}|_{\mathbf{q}_0}$ is the linearised operator around the steady-state, which herein is obtained with algorithmic differentiation, so it corresponds to the discrete linearisation. Similarly, operators $\mathbf{m}_\theta$, $\mathbf{m}_{\dot{\theta}}$ and $\mathbf{m}_{\dot{h}}$ are the linearised operators with respect to the structural degrees of freedom. The expression of the moment and lift coefficients $(C_M(\hat{\mathbf{q}}), C_L(\hat{\mathbf{q}}))$ is provided in the RHS of eq. (2.9), and the operators $\mathbf{c}_L^T$ and $\mathbf{c}_m^T$ are the

linear mappings between the perturbed state $\hat{\mathbf{q}}$ and the corresponding force or moment coefficient.

An efficient method to determine the eigenvalues of eq. (2.9) consists in the factorisation of the fluid system with respect to the structural degrees of freedom and to use the superposition principle to reconstruct the RHS of the structural equations, that is,

$$\begin{gathered}\mathbf{c}_L^T\hat{\mathbf{q}} = \mathbf{c}_L^T\sum_i \mathcal{R}(\lambda)\mathbf{m}_i, \quad \mathbf{c}_m^T\hat{\mathbf{q}} = \mathbf{c}_m^T\sum_i \mathcal{R}(\lambda)\mathbf{m}_i \text{ for } i = [\theta, \dot{\theta}, \dot{h}] \\ \text{where } Z_L^i(\lambda) = -\mathbf{c}_L^T\mathcal{R}(\lambda)\mathbf{m}_i, Z_m^i(\lambda) = -\mathbf{c}_m^T\mathcal{R}(\lambda)\mathbf{m}_i,\end{gathered} \tag{2.10}$$

which leads to the resolution of the following characteristic polynomial,

$$H(\lambda) = \begin{vmatrix} \lambda^2 + \left(2\zeta_h\left(\frac{\Omega^*}{U^*}\right) + \frac{Z_L^{\dot{h}}(\lambda)}{\overline{m}}\right)\lambda + \left(\frac{\Omega^*}{U^*}\right)^2 & \frac{Z_L^{\theta}(\lambda) + \lambda Z_L^{\dot{\theta}}(\lambda)}{\overline{m}} \\ \frac{\lambda Z_m^{\dot{h}}(\lambda)}{r_\theta^2\overline{m}} & \lambda^2 + \left(2\zeta_\theta\left(\frac{1}{U^*}\right) + \frac{Z_L^{\theta}(\lambda)}{\overline{m}}\right)\lambda + \left(\frac{1}{U^*}\right)^2 \end{vmatrix}. \tag{2.11}$$

The zeros of $H(\lambda)$ correspond to the eigenvalues of eq. (2.9). However, this process is not significantly more efficient than the direct computation of the eigenvalues of eq. (2.9). In order to determine the zeros of $H(\lambda)$ one needs to solve as many as structural degrees of freedom, three in our case, for each $\lambda \in \mathbb{C}$, as it was done by Sabino (2022).

However, the procedure can be considerably improved if one determine the transfer functions $Z_L^i(\mathrm{i}\omega)$ and $Z_m^i(\mathrm{i}\omega)$ for $i = [\theta, \dot{\theta}, \dot{h}]$, also known as impedances, along the real axis, that is, for $\lambda = \mathrm{i}\omega$ for $\omega \in \mathbb{R}$. Then, we reconstruct the complex form of the transfer functions using rational interpolation within the Loewner framework (Benner *et al.* 2017, Ch. 8). The Loewner framework provides a rigorous mathematical foundation for analytical continuation from measured frequency response data into the complex plane, making it particularly suited for dynamical systems identification. Its theoretical justification stems from tangential interpolation theory and realization theory for linear time-invariant (LTI) systems, where the rank property of the structured Loewner matrix directly reveals the minimal system order (Mayo & Antoulas 2007). Such a procedure, offers very good results in a thin region around the real axis where the transfer functions have been computed. Another advantage of this approach is that now one not only has an expression of $H(\lambda)$ but also $\dfrac{dH(\lambda)}{d\lambda}$, which enables fast computations of the eigenvalues using the Newton method.

Let us summarise the numerical procedure:

- Compute the transfer functions $Z_L^i(\mathrm{i}\omega)$ and $Z_m^i(\mathrm{i}\omega)$ for $i = [\theta, \dot{\theta}, \dot{h}]$, for $\omega \in \mathbb{R}$.
- Perform a rational interpolation following the Loewner framework, that is, compute $\tilde{Z}_L^i(\lambda), \tilde{Z}_m^i(\lambda)$ from $Z_L^i(\mathrm{i}\omega)$ and $Z_m^i(\mathrm{i}\omega)$ and determine $H(\lambda)$ using the rational interpolators.
- Determine the zeros of eq. (2.11) with the Newton method using the rational interpolators of the transfer functions, that is,

$$\delta\lambda_{n+1} = -\left(\frac{dH(\lambda)}{d\lambda}\right)^{-1}H(\lambda_n) \text{ with } \lambda_{n+1} = \lambda_n + \delta\lambda_{n+1} \tag{2.12}$$

In addition, for the computation of EP_n exceptional points, it is required that

$$\frac{d^jH(\lambda)}{d\lambda^j} = 0 \text{ for } j = 1, \ldots, n-1 \tag{2.13}$$

Case	U^* $\frac{U_\infty}{L\sqrt{K_\theta/I_{ca}}}$	Ω $\sqrt{\frac{K_h/m}{K_\theta/I_{ca}}}$	ζ_h $\frac{C_h}{2\sqrt{mK_h}}$	ζ_θ $\frac{C_\theta}{2\sqrt{I_{ca}K_\theta}}$	r_θ $\sqrt{\frac{I_{ca}}{mL^2}}$	x_θ $\frac{x_{cg}}{L}$	$\tilde{m}$ $\frac{m}{1/2\rho_f L^2}$	Re $\frac{\rho_f U_\infty L}{\mu}$	M_∞ $\frac{U_\infty}{c_\infty}$
Configuration (a)	$10^{-2}-1$	1.0	$D_s\frac{U^*}{\Omega}$	–	–	0	2.0	50	0.1
Configuration (b)	$10^{-2}-10^{1}$	0.8	0 – 0.2	0.05	0.290	0	10^3	2900	0.1
Configuration (c)	$0.5-10^{1}$	0.8	0 – 0.2	0.0 – 0.2	0.6	0	10^3	$3.2\cdot10^6$	0.73

Table 1. Values of dimensionless parameters and definition. For the cylinder the damping parameter D_s is varied between $[0, 1]$.

In such a case the eigenvalue condition $H(\lambda) = 0$ is complemented with the EP_n condition eq. (2.13) and it can be solved using a Newton update as for eq. (2.12).

3. Results

3.1. *Vortex-Induced-Vibrations for the flow past a circular*

We analyse the interplay between the fluid and VIV instabilities past a freely vertically moving circular cylinder at a $Re = 50$. The transfer function is represented in fig. 2 (a-b) for several values of the growth rate $\sigma = [0, -0.02, -0.04]$. The criterion for neutrality of the eigenvalue, that is, $\lambda = \mathrm{i}\omega$ is the following,

$$\underbrace{\mathrm{Re}\left(Z_L^{\dot{h}}(\mathrm{i}\omega)\right)}_{\text{aerodynamic damping}} = -2\zeta_h\frac{\Omega}{U^\star} = -D_s, \qquad \underbrace{\left(\overline{m} + \frac{\overbrace{\mathrm{Im}\left(Z_L^{\dot{h}}(\mathrm{i}\omega)\right)}^{\text{added mass}}}{\omega}\right)}_{\text{effective mass}}\omega^2 = \left(\frac{\Omega}{U^*}\right)^2. \tag{3.1}$$

That is, the aerodynamic damping must counterbalance the effect of the structural damping whereas the effective inertia due to the added mass must match the structural stiffness ($K_s = \left(\frac{\Omega}{U^*}\right)^2$). These two cases are represented in fig. 2 (a-b). The case $D_s = 0$ is represented with a dark blue line, in this case we can observe two intersections, one at a low frequency (ω_{LF}) which corresponds to the critical frequency of the fluid mode and a second at a higher frequency (ω_{HF}), which corresponds to the frequency where the heaving mode becomes unstable. In the second case, $D_s = 1$ which is represented with a dark green line, we can also observe two intersections at two very close frequencies. However, in this case both intersections belong to the fluid mode, while the heaving mode always remains stable. These two cases exemplify the behaviour on two opposite sides of the EP. For the first case, $D_s = 0$ which is represented in fig. 2 (c), the growth rate curves cross and the frequency curves are repelled. In contrast, for the second case where $D_s = 1$ and that is represented in fig. 2 (d), the growth rate curves are repelled and the frequency curves cross.

This phenomenon is further explored in fig. 2 (e), which represents the path of both modes for several values of the structural damping parameter $D_s = \{0, 0.8, 0.9, 1\}$ as a function of the reduced velocity. Therein, we can clearly observe a saddle-node at around $(\omega_{EP}, \sigma_{EP}) \approx (0.82, -0.02)$. For the values of the structural damping $D_s = \{0, 0.8\}$ the heaving mode becomes unstable and follows a trajectory to the right of the EP, while the fluid mode remains to the left of the EP and its growth rate decreases with U^*. For the highest values of the structural damping, $D_s = \{0.9, 1\}$, the heaving mode remains stable

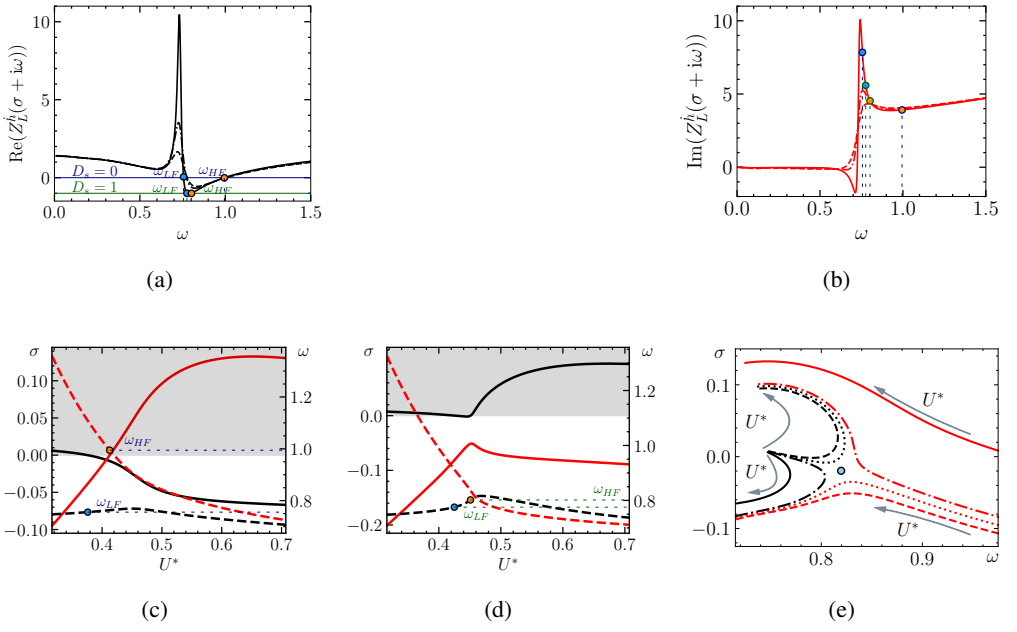

Figure 2. (a-b) Evolution of the transfer function Z_L^h with respect to the pulsation ω. The real part is represented in black (a) and the imaginary in red (b). Three growth rates σ are represented: $\sigma = 0$ (solid), $\sigma = -0.02$ (dashed) and $\sigma = -0.04$ (dash-dotted). (c) Evolution of the growth rate for $D_s = \zeta_h = 0$ for the fluid mode (black solid) and the heaving mode (red solid); the corresponding frequencies are shown with dashed lines. (d) The same as the middle figure but for $D_s = 1$. (e) Representation of path followed by the eigenvalues for increasing U^* for the fluid mode (black) and heaving mode (red) for $D_s = 0$ (solid), $D_s = 0.8$ (dash-dotted), $D_s = 0.9$ (dotted) and $D_s = 1.0$ (dashed). The exceptional point is represented with a light blue marker.

all along its trajectory and the growth rate of the fluid mode increases with the reduced velocity. For frequencies smaller than the one of the EP ($\omega < \omega_{EP}$), the fluid mode (resp. heaving mode) follows a similar trajectory to the heaving mode (resp. fluid mode) at lower structural damping.

This exchange is further exemplified in fig. 3. It represents the trajectory of eigenvalues along closed loops in the parameter space, in particular, along ellipses: $D_s = D_{s,EP} + r_{D_s}\cos(\theta)$ and $U^* = U^* + r_{U^*}\sin(\theta)$. It reveals the manifold structure of the exceptional point, in particular it shows that its winding number is half, that is, winding around the EP once induces a exchange of modes, while winding twice around the EP returns to the same eigenvalue branch. Thus, it is clear that the naming convention of heaving and fluid mode is just a convention, and it is arbitrary near a EP.

3.2. *Flutter instability for the flow past a thin plate*

In this section we explore the aeroelastic instabilities for the laminar flow past a thin plate (Moulin 2020). Figure 4 (a-b) shows the evolution of the two elastic modes as a function of the reduced velocity for $\zeta_h = 0$ (solid) and $\zeta_H = 0.03$ (dashed). The red lines represent the path of the heaving mode, and the black lines represent the evolution of the pitching mode. As it was the case for the VIV instability past the circular cylinder in section 3.1, the naming convention is somehow arbitrary in the region of the parameter space near the EP, that is when the two eigenvalue paths are attracted. Figure 4 displays the saddle-node structure that is observed around the EP. For values of the structural damping lower than

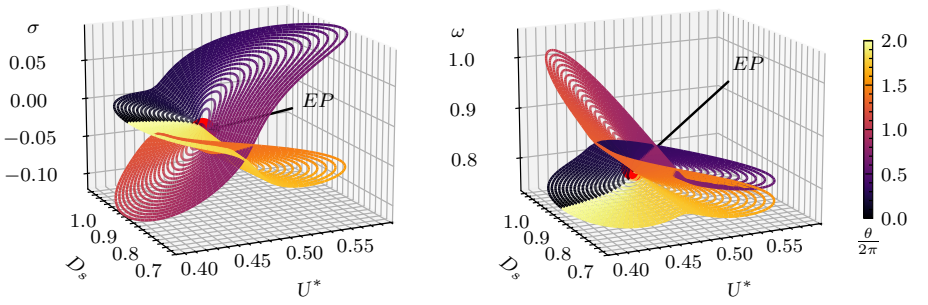

Figure 3. Manifold structure of the EP. It has been computed using individual trajectories along ellipses in the parameter space: $D_s = D_{s,EP} + r_{D_s}\cos(\theta)$ and $U^* = U^*_{EP} + r_{U^*}\sin(\theta)$ for $\theta \in [0, 4\pi]$, $r_{Ds} \in [0.001, 0.2]$ and $r_{U^*} \in [0.01, 0.1]$. The manifold is parametetrised by θ which is colour-coded. The EP is represented by a red circular marker.

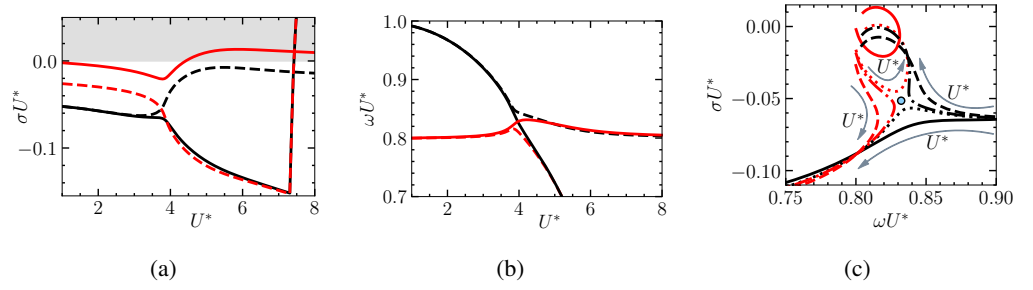

(a) (b) (c)

Figure 4. Evolution of the growth rate (a) and frequency (b) of the two elastic modes: heaving (red) and pitching (black) as a function of the reduced velocity for $\zeta_h = 0$ (solid) and $\zeta_h = 0.03$ (dashed). (c) Representation of path followed by the eigenvalues for increasing U^* for the pitching mode (black) and heaving mode (red) for $\zeta_h = 0$ (solid), $\zeta_h = 0.0175$ (dotted), $\zeta_h = 0.02$ (dash-dotted) and $\zeta_h = 0.03$ (dashed). The exceptional point is represented with a light blue marker.

$\zeta_{h,EP}$ the branch of the heaving mode becomes unstable and the pitching mode remains stable for a wide range of the reduced velocity but it eventually becomes unstable at the divergence reduced velocity, around $U^*_D \approx 7.4$. For $\zeta_h > \zeta_{h,EP}$ the growth rate of the branch of the pitching mode increases for reduced velocities higher than the ones of the U^*_{EP} and its frequency $\omega U^* \approx 0.8$, which corresponds to the one of the heaving mode, and in this the growth rate and frequency of the heaving branch decreases for a wide range of the reduced velocity until the divergence velocity $U^*_D \approx 7.4$ where it is destabilised. Such a mode-exchange occurs in the neighbourhood of the EP.

In order to demonstrate the mode-exchange, we represent the manifold structure of the EP in fig. 5. As in the VIV case discussed in section 3.1 it corresponds to a simple EP with a winding number equal to a half, that is, it takes two turns to return to the initial position. A single turn induces a mode-exchange. The important difference with the VIV case, it is the nature of the two modes. In this example, it corresponds to two aeroelastic modes, while in the case of the cylinder it is the coupling between a fluid and an aeroelastic mode. However, in both cases the underlying structure of the EP is the same.

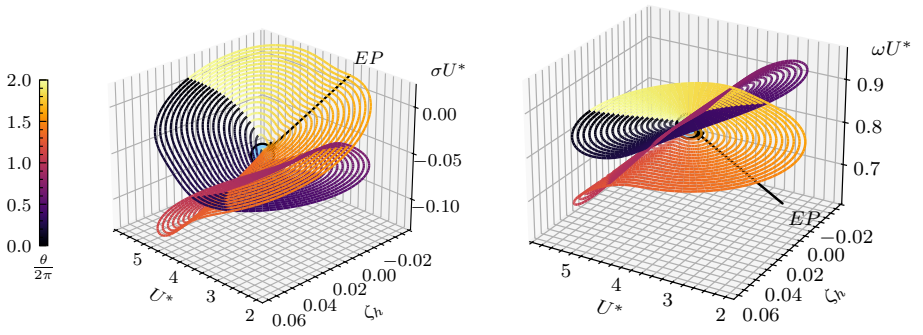

Figure 5. Manifold structure of the EP. It has been computed using individual trajectories along ellipses in the parameter space: $\zeta_h = \zeta_{h,EP} + r_{\zeta_h}\cos(\theta)$ and $U^* = U^*_{EP} + r_{U^*}\sin(\theta)$ for $\theta \in [0, 4\pi]$, $r_{U^*} \in [0.01, 2]$ and $r_{\zeta_h} \in [0.001, 0.05]$. The manifold is parametetrised by θ which is colour-coded. The EP is represented by a light blue circular marker.

3.3. *Transonic flutter instability past a OAT-15a airfoil*

In this last example, we illustrate the phenomenon of flutter in the transonic regime and in particular how two exceptional points drive the phenomenon known as *transonic dip* in aeroelasticity (Plath 2024, Sec. 1.2.2). To illustrate this phenomenon, we have selected the flow past the OAT15a airfoil at $M = 0.73$, $Re = 3.2 \cdot 10^6$ and $\alpha = 3.5°$, which has been previously studied in the fixed configuration by Sartor *et al.* (2015); Paladini *et al.* (2019), among others.

Figure 6 displays the spectrum for the structural values listed in table 1 (Conf. 3), $\zeta_h = 0.04273$, $\zeta_\theta = 0.0159$ and $U^* = 1$. The naming convention follows their behaviour at small reduced velocity, in particular if the displacement (resp. vertical velocity) is dominantly due to heaving, pitching motion or if it is small in comparison to the flow perturbations. The displacement (resp. velocity is represented) by red (resp. black) arrows on the right panel, where the norm of the mode has been normalised such the Chu's energy of the flow field is unitary. The left figure shows three leading eigenvalues, the fluid or buffet, the pitching and heaving modes represented with the blue, black and red markers respectively.

This configuration is further explored in fig. 7, which follows the path of the three leading eigenvalues while increasing the reduced velocity U^*, represented with the grey arrows. On fig. 7 (a) displays the selected configuration of damping parameters, and it shows two exceptional points of second order (EP_2). The first $EP_2^{f,h}$ leads to the interaction / exchange between the fluid and heaving mode and the second $EP_2^{f,p}$ between the pitching and fluid mode. The other four panels show the eigenvalue loci while varying the reduced velocity but with perturbed damping parameters, $\zeta_h = 0.04273 + r\cos(\theta)$, $\zeta_\theta = 0.0159 + r\sin(\theta)$ for $r = 0.0159$. On the panel (b) we can observe a mode exchange between the fluid and pitching mode around the exceptional point ($EP_2^{f,p}$) and the heaving branch is weakly deflected around the first exceptional point ($EP_2^{f,h}$). The panel (c) is very similar to the original one (a) but the interaction between the pitching and fluid mode is weaker and they do not exchange. On the panel (d) there is a mode exchange between the fluid and heaving mode around $EP_2^{f,h}$, and a strong interaction between the heaving and the pitching branches. Finally, on the panel (e) we have two mode switchings: first the heaving and fluid modes are swapped in a region close to around $EP_2^{f,h}$ and then there is a second mode

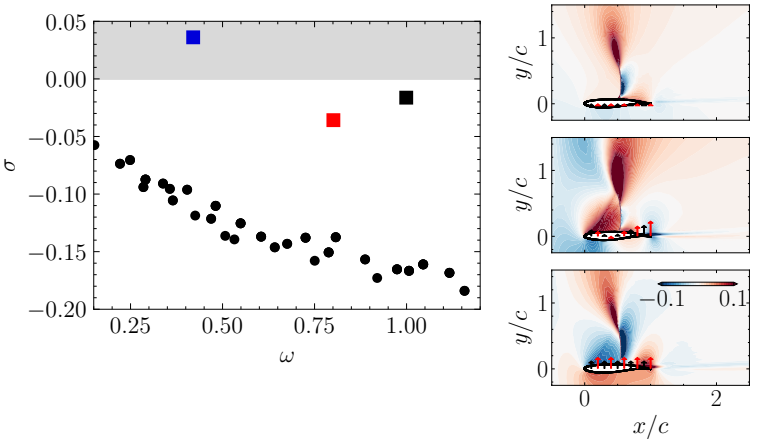

Figure 6. Spectrum for the configuration values listed in table 1 (Conf. 3) for $\zeta_h = 0.04273$, $\zeta_\theta = 0.0159$ and $U^* = 1$. The blue squared marker highlights the fluid mode, displayed on the top figure of the right panel. The pitching mode is represented with the black squared marker and on the middle figure of the right panel. The red squared marker represents the heaving mode, which is displayed on the bottom figure of the right panel. The red (resp. black) arrows of the right panel represent the vertical displacement (resp. velocity).

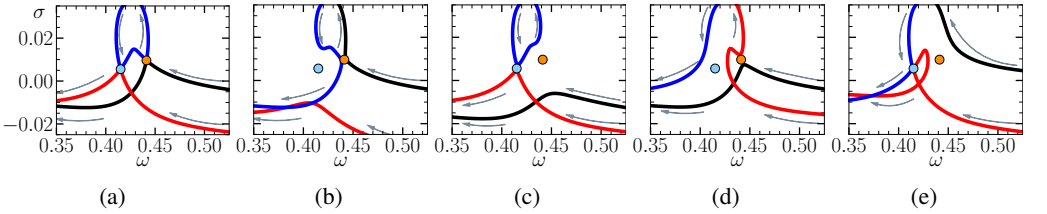

Figure 7. Veering phenomenon of the three leading eigenvalues: black line (pitching mode), red line (heaving mode) and blue line (fluid mode) around two exceptional points represented by two circle markers (blue and orange). Subfigure (a) is computed for $\zeta_h = 0.04273$, $\zeta_\theta = 0.0159$. Subfigures (b-e) are computed for damping parameters $\zeta_h = 0.04273 + r\cos(\theta)$, $\zeta_\theta = 0.0159 + r\sin(\theta)$ for $r = 0.0159$ and $\theta = 0$ for (b), $\theta = \pi/2$ for (c), $\theta = \pi$ for (d) and $\theta = 3\pi/2$ for (e). The remaining parameters are summarised in table 1. The grey arrows indicate the the direction of increasing U^*.

exchange between the pitching and heaving branches; that is for large U^* the fluid, heaving, and pitching branches behave as the heaving, pitching, and fluid mode, respectively.

The existence of two EP_2 nearby in the parameter space suggests the existence of a EP_3, that is, a degenerate point where the three modes coalesce. This phenomenon is explored in figure fig. 8 (a), that shows the evolution of the two aforementioned exceptional points while varying Ω^*. It shows that the two branches of EP_2 converge towards a point around $\Omega^* \approx 0.897$. For larger values of Ω^*, while keeping $r_\theta = 0.6$ and $\overline{m} = 10^3$ there are no EP_2, so in a sense the EP_3 is the organizing centre of the linear dynamics leading to the mode switching phenomena. We have partially tracked the evolution of the EP_3 in the parameter space $(r_\theta, \overline{m})$.

In order to demonstrate the mode-exchange around the EP_3, we represent the manifold structure of the EP in fig. 9. In contrast to the previous visualisations of EP_2, which are codimension two, that is we can encircle EP_2 with a circle, an EP_3 is codimension four and it has to be encircled with a four-dimensional sphere (S^3). In fig. 9 we show a partial view of this encircling and we evidence the fact that we need to encircle the EP_3 three times in order to return to the initial position, while a turning around once or twice induces

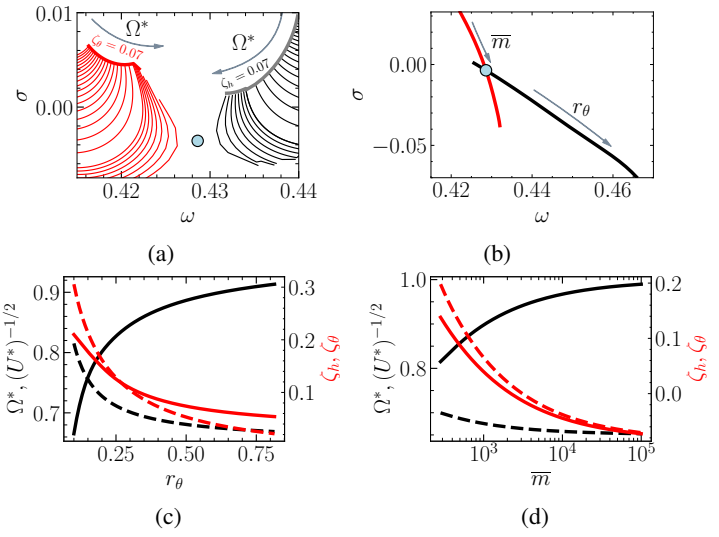

Figure 8. (a) Evolution of the $EP_2^{h,f}$ (thin red) as a function of (Ω^*, ζ_θ) and $EP_2^{p,f}$ (thin black) as a function of (Ω^*, ζ_h) with the upper computed limt of the damping parameter indicated with a thick line. The EP_3 is represented with a circle blue marker. (b) Represents the evolution of the EP_3 for varying reduced mass or r_θ while keeping the other constant. Evolution of the EP_3 as a function of $(r_\theta, \overline{m} = 10^3)$ (c) and as function of $(r_\theta = 0.6, \overline{m})$ (d).

a single or a double mode exchange. Encircling two EP_2 induces a similar sequence of mode-swapping, which justifies the analysis of the EP_3 in order to understand the sequence of mode exchanges and to label it as an organising centre.

4. Conclusion

This study has established exceptional points as a fundamental and organising feature in the linear stability spectrum of fluid-structure interaction systems. Through a consistent numerical and analytical framework applied to three archetypal configurations—vortex-induced vibration, incompressible plate flutter, and transonic airfoil flutter—we have demonstrated that the non-Hermitian nature of the coupled fluid-structure operator naturally gives rise to these spectral singularities.

In the VIV and plate flutter cases, the interaction between modes (fluid/structural or between two structural modes) creates second-order exceptional points (EP_2). These points act as topological pivots in parameter space, around which eigenvalue branches veer and exchange identities, a phenomenon characterised by a half-integer winding number. The stability landscape is thus fundamentally reshaped near an EP, where conventional modal labeling breaks down and the system exhibits enhanced sensitivity to parameters.

The transonic flutter configuration reveals a richer structure, where the close interplay between fluid (buffet), pitching, and heaving modes leads to the formation of two nearby EP_2s. These coalesce at a specific parameter set, giving rise to a third-order exceptional point (EP_3), where three eigenvalues and their eigenvectors simultaneously degenerate. This EP_3 acts as an organising centre for the complex mode-swapping patterns observed and is intrinsically linked to the pronounced loss of stability characteristic of the transonic dip.

The presence of EPs underscores that linear stability analyses in FSI must account for the possibility of eigenvalue degeneracies beyond the standard diagonalisable case.

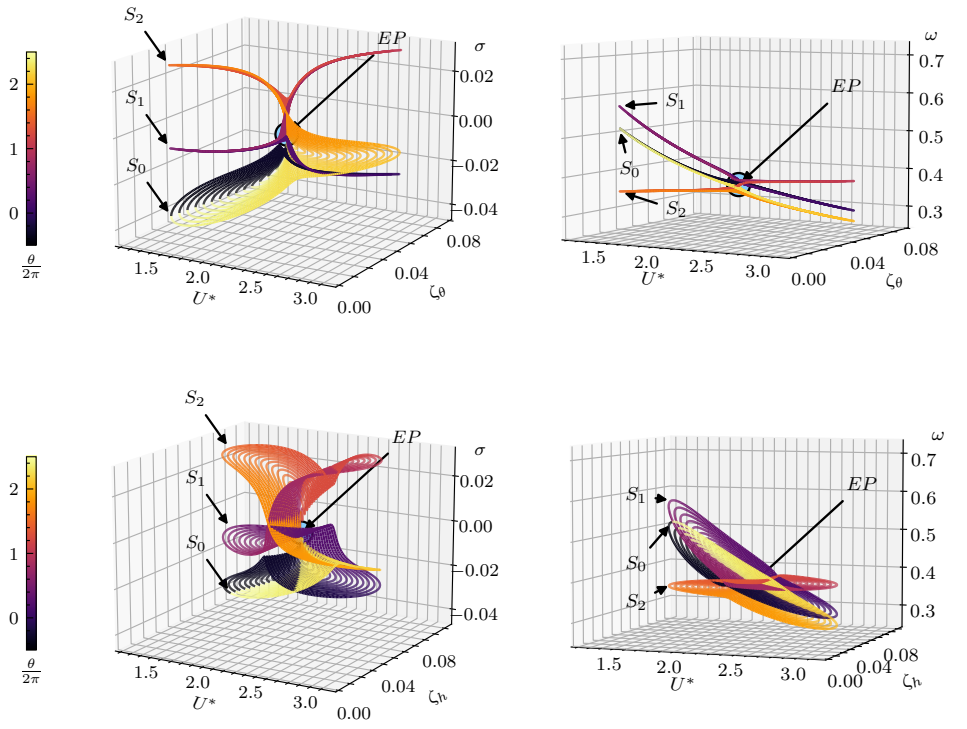

Figure 9. Manifold structure of the EP. It has been computed using individual trajectories along ellipses in the parameter space: $\zeta_h = \zeta_{h,EP} + r_{\zeta_h}\cos(\theta)$ and $U^* = U^*_{EP} + r_{U^*}\sin(\theta)$ for $\theta \in [0, 4\pi]$, $r_{U^*} \in [0.01, 2]$ and $r_{\zeta_h} \in [0.001, 0.05]$. The manifold is parametetrised by θ which is colour-coded. The EP is represented by a light blue circular marker.

The associated extreme parameter sensitivity and mode-swapping phenomena have direct implications for predicting flutter boundaries and for designing robust control strategies. Future work should explore exploiting the topological properties of EPs for novel flow control and energy harvesting paradigms, and investigate their role in nonlinear FSI dynamics and larger-scale dynamical systems.

References

Achilleos, Vassos, Theocharis, Georgios, Richoux, Olivier & Pagneux, Vincent 2017 Non-hermitian acoustic metamaterials: Role of exceptional points in sound absorption. *Physical Review B* **95** (14), 144303.

Aurégan, Yves & Pagneux, Vincent 2017 Pt-symmetric scattering in flow duct acoustics. *Physical review letters* **118** (17), 174301.

Benner, Peter, Ohlberger, Mario, Cohen, Albert & Willcox, Karen 2017 *Model reduction and approximation: theory and algorithms*. SIAM.

Bergholtz, Emil J, Budich, Jan Carl & Kunst, Flore K 2021 Exceptional topology of non-hermitian systems. *Reviews of Modern Physics* **93** (1), 015005.

Bonnefis, Paul, Sierra-Ausin, Javier, Fabre, David & Magnaudet, Jacques 2024 Path instability of deformable bubbles rising in newtonian liquids: a linear study. *Journal of Fluid Mechanics* **980**, A19.

Casel, Mario & Ghani, Abdulla 2024*a* A novel method for stable thermoacoustic system design based on exceptional points-part i: Conceptualization. *Combustion and Flame* **267**, 113559.

Casel, Mario & Ghani, Abdulla 2024*b* A novel method for stable thermoacoustic system design based on exceptional points-part ii: Application to laminar and turbulent flame configurations. *Combustion and Flame* **267**, 113558.

Doppler, Jörg, Mailybaev, Alexei A, Böhm, Julian, Kuhl, Ulrich, Girschik, Adrian, Libisch, Florian, Milburn, Thomas J, Rabl, Peter, Moiseyev, Nimrod & Rotter, Stefan 2016 Dynamically encircling an exceptional point for asymmetric mode switching. *Nature* **537** (7618), 76–79.

Feng, Liang, Wong, Zi Jing, Ma, Ren-Min, Wang, Yuan & Zhang, Xiang 2014 Single-mode laser by parity-time symmetry breaking. *Science* **346** (6212), 972–975.

Ghani, Abdulla & Polifke, Wolfgang 2021 An exceptional point switches stability of a thermoacoustic experiment. *Journal of Fluid Mechanics* **920**, R3.

Heiss, Walter D 2012 The physics of exceptional points. *Journal of Physics A: Mathematical and Theoretical* **45** (44), 444016.

Helbig, Tobias, Hofmann, Tobias, Imhof, S, Abdelghany, M, Kiessling, T, Molenkamp, LW, Lee, CH, Szameit, A, Greiter, M & Thomale, R 2020 Generalized bulk–boundary correspondence in non-hermitian topolectrical circuits. *Nature Physics* **16** (7), 747–750.

Humbert, Sylvain C & Orchini, Alessandro 2025 Symmetry-breaking induced exceptional points in the thermoacoustic spectrum of annular combustors. *Journal of Fluid Mechanics* **1009**, R5.

Jouin, Antoine, Ciola, Nicola, Cherubini, Stefania & Robinet, Jean Christophe 2024 Detuned secondary instabilities in three-dimensional boundary-layer flow. *Physical Review Fluids* **9** (4), 043901.

Kern, J Simon, Lupi, Valerio & Henningson, Dan S 2024 Floquet stability analysis of pulsatile flow in toroidal pipes. *Physical Review Fluids* **9** (4), 043906.

Li, Xiaopeng, Yu, Ziqi, Iizuka, Hideo & Lee, Taehwa 2022 Experimental demonstration of extremely asymmetric flexural wave absorption at the exceptional point. *Extreme Mechanics Letters* **52**, 101649.

Matsushima, Kei & Yamada, Takayuki 2025 Exceptional points and defective resonances in an acoustic scattering system with sound-hard obstacles. *Proceedings of the Royal Society A* **481** (2320), 20250230.

Mayo, AJ & Antoulas, Athanasios C 2007 A framework for the solution of the generalized realization problem. *Linear algebra and its applications* **425** (2-3), 634–662.

Mensah, Georg A, Magri, Luca, Silva, Camilo F, Buschmann, Philip E & Moeck, Jonas P 2018 Exceptional points in the thermoacoustic spectrum. *Journal of Sound and Vibration* **433**, 124–128.

Miri, Mohammad-Ali & Alu, Andrea 2019 Exceptional points in optics and photonics. *Science* **363** (6422), eaar7709.

Moulin, Johann 2020 On the flutter bifurcation in laminar flows: linear and nonlinear modal methods. PhD thesis, Institut polytechnique de Paris.

Orchini, Alessandro, Silva, Camilo F, Mensah, Georg A & Moeck, Jonas P 2020 Thermoacoustic modes of intrinsic and acoustic origin and their interplay with exceptional points. *Combustion and Flame* **211**, 83–95.

Paladini, Edorado, Beneddine, Samir, Dandois, Julien, Sipp, Denis & Robinet, Jean-Christophe 2019 Transonic buffet instability: From two-dimensional airfoils to three-dimensional swept wings. *Phys. Rev. Fluids* **4**, 103906.

Plath, Matthias 2024 Numerical aeroelastic stability of transonic laminar airfoils. PhD thesis, Université Paris-Saclay.

Sabino, Diogo 2022 Aeroelastic instabilities of an airfoil in transitional flow regimes. PhD thesis, Université Paul Sabatier-Toulouse III.

Sartor, Fulvio, Mettot, Clément & Sipp, Denis 2015 Stability, receptivity, and sensitivity analyses of buffeting transonic flow over a profile. *Aiaa Journal* **53** (7), 1980–1993.

Schaefer, Felicitas, Guo, Shuai & Polifke, Wolfgang 2021 The impact of exceptional points on the reliability of thermoacoustic stability analysis. *Journal of Engineering for Gas Turbines and Power* **143** (2), 021010.

Schmid, Peter J 2007 Nonmodal stability theory. *Annu. Rev. Fluid Mech.* **39** (1), 129–162.

Shi, Chengzhi, Dubois, Marc, Chen, Yun, Cheng, Lei, Ramezani, Hamidreza, Wang, Yuan & Zhang, Xiang 2016 Accessing the exceptional points of parity-time symmetric acoustics. *Nature communications* **7** (1), 11110.

Trefethen, Lloyd N, Trefethen, Anne E, Reddy, Satish C & Driscoll, Tobin A 1993 Hydrodynamic stability without eigenvalues. *Science* **261** (5121), 578–584.

Wiersig, Jan 2020 Review of exceptional point-based sensors. *Photonics research* **8** (9), 1457–1467.

Xiong, Lei, Nennig, Benoit, Aurégan, Yves & Bi, Wenping 2017 Sound attenuation optimization using metaporous materials tuned on exceptional points. *The Journal of the Acoustical Society of America* **142** (4), 2288–2297.

Yao, Shunyu & Wang, Zhong 2018 Edge states and topological invariants of non-hermitian systems. *Physical review letters* **121** (8), 086803.

Zhou, Hengyun, Peng, Chao, Yoon, Yoseob, Hsu, Chia Wei, Nelson, Keith A, Fu, Liang, Joannopoulos,

John D, Soljačić, Marin & Zhen, Bo 2018 Observation of bulk fermi arc and polarization half charge from paired exceptional points. *Science* **359** (6379), 1009–1012.

Zhu, Weiwei, Fang, Xinsheng, Li, Dongting, Sun, Yong, Li, Yong, Jing, Yun & Chen, Hong 2018 Simultaneous observation of a topological edge state and exceptional point in an open and non-hermitian acoustic system. *Physical review letters* **121** (12), 124501.